



The Compact UV Size of Green Pea Galaxies As Local Analogs of High-redshift Ly α -Emitters

Keunho J. Kim^{1,2} , Sangeeta Malhotra^{2,3} , James E. Rhoads^{2,3} , and Huan Yang⁴

¹Department of Physics, University of Cincinnati, Cincinnati, OH 45221, USA; kim2k8@ucmail.uc.edu

²School of Earth & Space Exploration, Arizona State University, Tempe, AZ 85287, USA

³NASA Goddard Space Flight Center, Greenbelt, MD 20771, USA

⁴Las Campanas Observatory, Carnegie Institution for Science, Chile

Received 2020 September 2; revised 2021 April 5; accepted 2021 April 13; published 2021 June 8

Abstract

We study the dependence of Ly α escape from galaxies on UV continuum size and luminosity using a sample of 40 Green Pea (GP) galaxies, which are the best local analogs of high-redshift Ly α emitters (LAEs). We use the Cosmic Origins Spectrograph near-ultraviolet images from the Hubble Space Telescope to measure the UV size and luminosity with 0".047 spatial resolution. Like most galaxies the GPs show a log-normal size distribution. They also show a positive correlation between size and UV-continuum luminosity. The slope of the size-continuum luminosity relation for GPs is consistent with those of continuum-selected star-forming galaxies (SFGs) at low and high redshifts. A distinctive feature of GPs is a very compact typical radius of 0.33 kpc with a population spread (1σ) of 0.19 kpc. The peak of the size distribution and the intercept of the size–luminosity relation of GPs are noticeably smaller than those of continuum-selected SFGs at similar redshifts. There are statistically significant anticorrelations found between the circularized half-light radius ($r_{\text{cir},50}$), the Ly α equivalent width (EW(Ly α)), and the Ly α escape fraction ($f_{\text{esc}}^{\text{Ly}\alpha}$), suggesting that small UV-continuum radii are crucial for Ly α emission. GPs and high-redshift LAEs have similar sizes, once spatial resolution effects are properly considered. Our results show that a compact small size is crucial for escape of Ly α photons, and that Ly α emitters show constant characteristic size independent of their redshift.

Unified Astronomy Thesaurus concepts: Compact galaxies (285); Starburst galaxies (1570); Galaxy formation (595); Galaxy evolution (594); Galaxy structure (622); Star formation (1569); Reionization (1383); Lyman alpha galaxies (978); Emission line galaxies (459)

1. Introduction

Ly α -emitting galaxies (i.e., Ly α -emitters, LAEs) are a class of galaxies characterized by spectra with prominent Ly α emission lines. Since Ly α photons are usually generated by intense star formation activity, most LAEs have relatively high star formation rate (SFR) for their stellar mass (i.e., specific star formation rate, $\text{sSFR} \gtrsim 10^{-8} \text{ yr}^{-1}$) and relatively young stellar population ages ($\lesssim 50$ Myr) (e.g., Malhotra & Rhoads 2002; Gawiser et al. 2007; Pirzkal et al. 2007; Finkelstein et al. 2015a; Santos et al. 2020). However, because Ly α photons are resonantly scattered by neutral hydrogen and significantly affected by dust absorption/scattering (e.g., Ahn et al. 2003), not all actively star-forming galaxies (SFGs) have observable Ly α emission, which requires that Ly α photons manage to escape from star-forming regions within the galaxy all the way to the intergalactic medium (IGM). So what are the properties of LAEs that allow Ly α to escape?

Ly α emission from galaxies is also one of the most promising indicators for identifying Lyman-continuum (LyC) leakers (i.e., galaxies that emit significant amounts of ionizing radiation to the IGM; Verhamme et al. 2015; de Barros et al. 2016; Izotov et al. 2016; Gazagnes et al. 2020). LyC leaking galaxies are important for cosmology, because they were significant and probably dominant sources of the photons that drove reionization of the early universe ($z > 6$). Thus, studying the physical properties of LAEs and understanding their Ly α (and potentially LyC) escape mechanisms have been important topics in the fields of galaxy evolution and cosmology, respectively (e.g., Malhotra & Rhoads 2002; Malhotra et al. 2012; Rhoads et al. 2000, 2014; Finkelstein et al. 2015a;

Oyarzún et al. 2017; Rivera-Thorsen et al. 2017, and references therein; Runnholm et al. 2020).

Multiple observations and morphological analysis of LAEs show that they are mostly compact (with effective radius $r_{\text{eff}} \lesssim 1.5$ kpc), sometimes with clumpy features shown in UV continuum, at high redshifts $2 \lesssim z \lesssim 7$ (e.g., Dow-Hygelund et al. 2007; Overzier et al. 2008; Bond et al. 2009; Taniguchi et al. 2009; Bond et al. 2012; Malhotra et al. 2012; Jiang et al. 2013; Paulino-Afonso et al. 2018; Ritondale et al. 2019; Shibuya et al. 2019). Based on the approximately constant typical sizes of LAEs over a wide span of redshift ($2 \lesssim z \lesssim 6$), Malhotra et al. (2012) suggested that the compact size of LAEs is a crucial physical condition for a galaxy to become an LAE, as recent analytic calculations on morphologically compact conditions for LyC leakers also suggest (Cen 2020). This has been supported by later studies (e.g., Jiang et al. 2013; Paulino-Afonso et al. 2018), but others (notably Shibuya et al. 2019) have challenged this with the view that LAEs follow similar size–luminosity relations, and show size evolution with redshift similar to high-redshift Lyman-break galaxies (LBGs). Among the LBG samples, moreover, it has been suggested that size evolution differs between brighter ($L_{\text{UV}} > 0.3L_*$) and fainter ($L_{\text{UV}} < 0.3L_*$) galaxies, where L_{UV} and L_* are the UV luminosity and the characteristic luminosity of galaxies, respectively (e.g., Bouwens et al. 2015; Finkelstein et al. 2015b).

Extending this redshift dependence to lower redshifts would give a more sensitive test of whether the characteristic radius of LAEs evolves like $(1+z)^{-1.37}$ (Shibuya et al. 2019) or is flat. Going from $z=6$ to 2 gives a factor of 3 change in the size while going to $z=0.3$ predicts more than a factor of 10 in

radius change. Green Peas (GPs) are the best low-redshift analogs of high-redshift LAEs in terms of Ly α equivalent width distribution (Yang et al. 2016). GPs were selected as high equivalent width [O III] emitters in a citizen science project, and have generally low metallicities and low masses (Cardamone et al. 2009; Amorín et al. 2010; Jaskot & Oey 2013; Henry et al. 2015; Izotov et al. 2016; Yang et al. 2016, 2017a, 2017b; Izotov et al. 2018; Orlitová et al. 2018; Jaskot et al. 2019; Jiang et al. 2019a, 2019b; Hogarth et al. 2020; Brunker et al. 2020; Clarke et al. 2021).

This is the second in a series of papers where we investigate the UV continuum morphologies of GP galaxies to understand the mechanisms enabling Ly α escape. In the first paper (Kim et al. 2020, hereafter Paper I) we investigated the effects of star formation per unit area, a.k.a., star formation intensity (SFI) and specific star formation rate (sSFR). In this paper we investigate the UV size and luminosity of a sample of GPs that were observed with the Cosmic Origins Spectrograph near-ultraviolet (COS/NUV) acquisition images from the HST. The high angular resolution of the COS/NUV images (0.0235 arcsec pixel⁻¹ sampling and PSF FWHM of 0.047 arcsec) and the low redshifts ($z=0.1\text{--}0.3$) of GPs have enabled us to measure the spatially resolved UV sizes with a factor of ~ 2 better resolution limit compared to other HST instrument+filter combinations typically used for measuring the sizes of high- z LAEs (i.e., 0.047 arcsec, versus 0.09 arcsec for the Advanced Camera for Surveys (ACS) F850LP filter, and 0.15 arcsec for the Wide Field Camera 3 (WFC3) F160W; Windhorst et al. 2011). We use this exquisite spatial resolution to test whether low-redshift LAEs have compact physical sizes, which would be expected if the small sizes of high- z LAEs are causally linked to Ly α escape. Alternatively, if high- z LAEs are compact merely because high- z galaxies are compact in general, we would expect their local counterparts to be larger. We also use our data set to study more general aspects of the relation between Ly α escape and UV continuum size.

Section 2 describes our galaxy sample and procedures for UV size and luminosity measurements. In Section 3, we present our results. We summarize our conclusions in Section 4. Throughout this paper, we adopt the AB magnitude system and the Λ CDM cosmology of $(H_0, \Omega_m, \Omega_\Lambda) = (70 \text{ km s}^{-1} \text{ Mpc}^{-1}, 0.3, 0.7)$.

2. Sample and Data Analysis

2.1. GP Sample

Our GP sample consists of the 40 galaxies with UV spectra that are analyzed and presented by Yang et al. (2017b; hereafter Y17) and Paper I. Our sample GPs have redshifts $0.1 \lesssim z \lesssim 0.35$. GPs were selected by citizen scientists for colors indicating a strong [O III] $\lambda 5007$ emission line in the SDSS r -band (Cardamone et al. 2009) and compact unresolved morphology at SDSS seeing of $1.2\text{--}2''$. The current sample excludes galaxies whose line ratios indicate an active galactic nucleus, based on the BPT diagram (Baldwin et al. 1981). As we will see in the next section, the measured NUV sizes of the GPs are much smaller than the SDSS seeing. Therefore, the citizen science criteria that GPs be “round” and “pea-like” do not bias the measured median sizes much.

The HST UV spectroscopy was drawn from several observing programs, but notably, about half this sample was new in Y17, and was selected to sample the range of metallicity and dust extinction as much as possible. Of the 43 GPs in Y17, we removed three galaxies—one (GP ID 0747+2336) that shows no

Ly α emission line, and two others (GP ID 0021+0052 and 0938+5428) where the COS imaging data were obtained using the MIRRORB instrument configuration.⁵ We refer to Y17 for further details on sample selection procedures.

We adopt GP ID and Ly α properties such as the equivalent width of Ly α line ($\text{EW}(\text{Ly}\alpha)$), the Ly α escape fraction ($f_{\text{esc}}^{\text{Ly}\alpha}$), and the Ly α luminosity ($L(\text{Ly}\alpha)$) from Y17. We also adopt galactic internal extinction (A_{int}), Milky Way extinction (A_{MW}), and the k -correction (k) values from Paper I to derive the extinction and k -corrected UV luminosity at rest-frame wavelength of 1877 Å of our sample GPs in Section 2.2.

As described in Paper I, the 40 sample GPs have been observed with the COS/NUV acquisition images with the MIRRORA configuration. The pivot wavelength of the observed filter is 2319.7 Å. The exposure time of the NUV images of our sample GPs is mostly greater than 100 s. For more details we refer the reader to Paper I.

2.2. Size and Luminosity Measurements

We measure the UV-continuum size and luminosity of our sample GPs using two different size measures: first, the Petrosian half-light radius (Petrosian 1976); and second, the effective radius measured from surface brightness profile fitting using the public software GALFIT (version 3.0.5; Peng et al. 2002, 2010). The Petrosian radius has certain advantages (described below) that led us to use it as our size measure of choice for most analyses in this study. The exception is Section 3.4, where we compare the typical size of GPs with those of high-redshift LAEs by employing the effective radius to ensure consistency between low- and high-redshift size measures.⁶

To measure the sizes, we first derive the galaxy center and apparent axis ratio b/a (where a and b indicate the semimajor and semiminor axis of a galaxy, respectively, and ellipticity $\epsilon = 1 - b/a$) by performing GALFIT surface brightness profile fitting. We adopt the same sky-subtracted 140×140 pixel ($3''3 \times 3''3$) COS/NUV images of our sample GPs and the point-spread function (PSF) image of star P330E observed during the HST program 11473 (see footnote 5) that we processed in Paper I to measure the central star formation intensity (SFI, star formation rate per unit area) of this sample. During the fitting procedure, we assume one component Sérsic profile, and the associated background noise σ images are internally generated by considering image information such as exposure time, readout noise, and the number of combined images from the image header. The initial guesses for galaxy center, apparent magnitude, and the effective radius are adopted from the measured values in Paper I. Specifically, the brightest pixel of the NUV images, and the Petrosian-based galaxy segmentation maps and the pixel-count based size parameter (Petrosian 1976; Law et al. 2007; Ribeiro et al. 2016) are used to obtain initial values of the galaxy center, apparent magnitude, and effective radius. The initial values for b/a and Position Angle (i.e., the direction of galaxy major axis in

⁵ http://www.stsci.edu/hst/cos/documents/isrs/ISR2010_10.pdf

⁶ We note that there is a systematic size difference between the two size measures (i.e., Petrosian half-light radius and the effective radius) depending on the concentration of the galaxy’s light profile (i.e., Sérsic index) (Graham & Driver 2005; Graham et al. 2005). We checked that both size measures of our sample GPs give qualitatively similar results throughout our analysis, though the effective radius has a broader size distribution with a higher median size compared to the Petrosian half-light radius (i.e., the median effective radius is ~ 0.62 kpc, while the median Petrosian half-light radius is ~ 0.33 kpc).

the sky) are set to 0.8 and 0 degrees, respectively, for all sample galaxies.

Additionally, we put constraints on the fitting range of some parameters. A fitting solution for this type of multiparameter fit does not always guarantee a physically sound result, even with a reasonably good reduced- χ^2 value (e.g., Peng et al. 2010; Meert et al. 2015; Kim et al. 2016, for relevant discussions). Therefore, to make sure that the fits are physically motivated, the fitted galaxy center is to be within 5 pixels from the initial galaxy center; the effective radius is greater than 1 pixel but less than twice the total radius derived from the galaxy size parameter mentioned above; the Sérsic index is between 1 and 8; and the b/a value is fit between 0.2 and 1.

From the fit results, we employ the galaxy center, apparent axis ratio (b/a), and the position angle to measure the Petrosian radius and luminosity. Since the Petrosian radius depends on the surface brightness profile (i.e., a curve of growth) of a galaxy, this size definition has the advantages of being redshift independent, less sensitive to dust reddening, and insensitive to variations in the signal-to-noise ratio and in the limiting surface brightness of the observations (Petrosian 1976; Lotz et al. 2004). The Petrosian radius r_p is defined to be the radius at which the surface brightness $\mu(r_p)$ is equal to a factor of η times the mean surface brightness $\bar{\mu}(r < r_p)$ within the r_p . That is, $\mu(r_p) = \eta \times \bar{\mu}(r < r_p)$. A constant η value is typically set to 0.2 (e.g., Petrosian 1976; Conselice et al. 2000; Shimasaku et al. 2001; Lotz et al. 2004; Guaita et al. 2015). We adopt the same η value of 0.2 for our size measurement.

To solve for the above Petrosian equation, we measure the surface brightness profile of galaxies by performing the IRAF ellipse task. To account for the PSF effect on the Petrosian radius measurement, we adopt the same PSF-deconvolved and sky-subtracted COS/NUV images that we processed in Paper I (see Section 2.2 for details). During the ellipse task, we fix the galaxy center and the ellipticity ϵ with the values obtained from the GALFIT results. The measured surface brightness profile of sample GPs is used to find the r_p . The exact value of r_p is calculated by first finding the two closest radii to r_p at which the surface brightnesses are measured, and then performing linear interpolation or extrapolation with these two closest radii to derive the exact r_p that satisfies the Petrosian equation.

The typical difference between the exact value of r_p derived and the two closest radii found in the measured surface brightness profile is only 0.22 pixels (equivalently 0.0052 arcsec). This small interpolation/extrapolation corresponds to the $\sim 4\%$ relative difference between the derived r_p and the two closest radii (that is, $1 - (r_{cl}/r_p) \sim 0.04$ where r_{cl} is the mean radius of the two closest radii). Therefore, we do not expect the details of our interpolation procedure (e.g., the polynomial degree used) to significantly change our measured sizes.

We subsequently measure the UV-continuum luminosity L_p and the Petrosian half-light radius r_{50} based on the r_p by following the conventional definitions of L_p and r_{50} (e.g., Shimasaku et al. 2001). The L_p is defined to be the total flux within the enclosed area of $2r_p$ from galaxy center, and the r_{50} to be the radius within which half of L_p is enclosed. As in the r_p measurement, we perform the same linear interpolation/extrapolation to derive the exact values of L_p and r_{50} . The measured r_{50} of our sample GPs in pixel unit ranges from 2 pixel $\lesssim r_{50} \lesssim$ 17 pixel, with a median of 4.1 pixel, first and third quartile values of 2.6 pixel and 6.4 pixel, and a standard deviation of 3.1 pixel. The measurement uncertainties in L_p are derived considering the Poisson statistics

(i.e., photon counting statistics) and propagation of the errors during the image calibration procedures such as flat-field correction obtained from the provided COS/NUV error images. For uncertainties in r_{50} , we adopted the derived fractional uncertainty of half-light radius based on median statistics and the associated aperture photometry uncertainty for LAEs at $z \sim 2-3$ in Bond et al. (2012). The typical measurement uncertainties in L_p and r_{50} in our sample GPs are 0.02 mag and 0.01 kpc, respectively.

Lastly, the measured L_p is corrected for galactic internal extinction (A_{int}), Milky Way extinction (A_{MW}), and the k -correction (k) with the values obtained from Paper I (see Section 2.1 for details). By adopting the characteristic luminosity at $z \sim 3$ ($L_{*,z=3}$) which corresponds to UV magnitude of -21 , the L_p of our sample GPs ranges from $0.1L_{*,z=3}$ to $2.4L_{*,z=3}$, with a median L_p of $0.64L_{*,z=3}$. We also calculate the circularized half-light radius (i.e., $r_{\text{cir},50} = r_{50} \times \sqrt{b/a}$) and the circularized effective radius ($r_{\text{cir,eff}} = r_{\text{eff}} \times \sqrt{b/a}$, where r_{eff} is the effective radius along the major axis), respectively. The measured r_p , r_{50} , $r_{\text{cir},50}$, $r_{\text{cir,eff}}$, Sérsic index, b/a , and L_p as well as the adopted extinction (A_{int} and A_{MW}) and k -correction (k) values are listed in Table 1.

3. Results and Discussion

3.1. Size Distribution of GPs

In this section, we investigate the UV size distribution of our sample GPs. Figure 1 shows the distributions of $r_{\text{cir},50}$ (left panel) and of $r_{\text{cir},50}$ versus redshift (right panel), respectively. The left panel shows that our sample GPs show mostly small UV sizes with a median $r_{\text{cir},50}$ of 0.33 kpc and a 1σ spread of 0.19 kpc, marked as the vertical dashed line and the horizontal solid line, respectively. The size distribution is relatively narrow as its semi-interquartile range is only 0.13 kpc. The mean $r_{\text{cir},50}$ of 0.36 kpc is larger than the median, due to the presence of a long tail toward large sizes as shown in the left panel of the figure.⁷ The right panel shows the size versus redshift distribution. Compared to the typical PSF FWHM of COS/NUV images (i.e., the blue solid line), it shows that the sizes of sample GPs are mostly resolved with the NUV images.

We also fit the size distribution of our sample GPs with a log-normal distribution:

$$p(r_{\text{cir},50}) = \frac{1}{\sigma_{\ln(r_{\text{cir},50})} r_{\text{cir},50} \sqrt{2\pi}} \exp \left[-\frac{\ln^2(r_{\text{cir},50}/r_{\text{med}})}{2\sigma_{\ln(r_{\text{cir},50})}^2} \right], \quad (1)$$

where $p(r_{\text{cir},50})$ is the log-normal probability density function of $r_{\text{cir},50}$. Here r_{med} and $\sigma_{\ln(r_{\text{cir},50})}$ are the median size and the width of the fitted log-normal distribution, respectively. As shown in the left panel of the figure, the size distribution of our sample GPs is well fitted by a log-normal function (i.e., dotted line) with the associated $r_{\text{med}} = 0.32$ kpc and $\sigma_{\ln(r_{\text{cir},50})} = 0.47$.

A relevant interpretation of the log-normal distribution of galaxy size might come from theoretical galaxy disk formation

⁷ The typical size of our sample GPs (i.e., the median $r_{\text{cir},50}$ of 0.33 kpc) corresponds to the angular size of ~ 0.1 arcsec at the typical redshift of 0.25 of our sample GPs. We note that the measured small size of our sample GPs does not result from potential sample selection bias as our sample GPs were drawn, without imposing size criteria, from the parent sample GPs whose SDSS image has a significantly larger seeing cutoff of $\gtrsim 1$ arcsec that corresponds to ~ 5 kpc at their typical redshifts (see Section 2.3 of Cardamone et al. 2009 for further details).

Table 1
The Measured Parameters of Sample Galaxies

Green Pea ID ^a	SDSS ObjID ^b	$m_{UV}^{c,d}$ (mag)	$M_{UV}^{c,d}$ (mag)	$r_{cir,50}^{f,g}$ (arcsec)	$r_{cir,50}^{h,g}$ (kpc)	$r_{cir,p}^{i,g}$ (arcsec)	$r_{cir,p}^{j,g}$ (kpc)	$r_{cir,eff}^k$ (arcsec)	$r_{cir,eff}^l$ (kpc)	n^m	b/a^n	A_{int}^o (mag)	A_{MW}^p (mag)	k^q (mag)
0055-0021	1237663783666581565	19.85 ± 0.03	-20.59 ± 0.03	0.233 ± 0.006	0.509 ± 0.016	0.526 ± 0.013	1.147 ± 0.037	0.152 ± 0.009	0.435 ± 0.019	1.00 ± 0.18	0.58 ± 0.07	0.85	0.184	0.123
0303-0759	1237652900231053501	20.73 ± 0.02	-19.35 ± 0.02	0.072 ± 0.001	0.177 ± 0.003	0.173 ± 0.002	0.424 ± 0.006	0.212 ± 0.010	0.599 ± 0.025	8.00 ± 0.25	0.75 ± 0.01	0	0.716	0.128
0339-0725	1237649961383493869	19.97 ± 0.02	-21.51 ± 0.02	0.149 ± 0.002	0.493 ± 0.007	0.289 ± 0.004	0.954 ± 0.014	0.213 ± 0.006	0.859 ± 0.020	3.38 ± 0.10	0.67 ± 0.01	0.387	0.447	-0.043
0749+3337	1237674366992646574	20.07 ± 0.02	-21.95 ± 0.02	0.227 ± 0.003	0.628 ± 0.011	0.345 ± 0.004	0.954 ± 0.017	0.308 ± 0.011	1.284 ± 0.029	3.52 ± 0.07	0.44 ± 0.01	0.832	0.405	-0.065
0751+1638	1237673807042708368	21.43 ± 0.03	-20.14 ± 0.03	0.127 ± 0.003	0.418 ± 0.012	0.262 ± 0.006	0.862 ± 0.024	0.383 ± 0.055	1.560 ± 0.182	6.84 ± 0.50	0.65 ± 0.02	0.609	0.264	-0.050
0805+0925	1237667729656905788	21.55 ± 0.03	-21.65 ± 0.03	0.128 ± 0.003	0.543 ± 0.014	0.247 ± 0.006	1.044 ± 0.027	0.315 ± 0.037	1.498 ± 0.156	5.20 ± 0.39	0.79 ± 0.03	1.686	0.154	-0.160
0815+2156	1237664668421849521	20.75 ± 0.01	-18.54 ± 0.01	0.060 ± 0.001	0.128 ± 0.002	0.138 ± 0.001	0.294 ± 0.003	0.205 ± 0.010	0.510 ± 0.021	8.00 ± 0.26	0.74 ± 0.01	0.054	0.298	0.173
0822+2241	1237664092897083648	20.80 ± 0.02	-20.42 ± 0.02	0.076 ± 0.002	0.251 ± 0.005	0.133 ± 0.003	0.437 ± 0.008	0.284 ± 0.024	0.997 ± 0.08	8.00 ± 0.44	0.88 ± 0.02	0.781	0.329	0.035
0911+1831	1237667429018697946	20.53 ± 0.01	-21.03 ± 0.01	0.074 ± 0.007	0.252 ± 0.003	0.146 ± 0.002	0.494 ± 0.006	0.136 ± 0.004	0.552 ± 0.014	8.00 ± 0.23	0.70 ± 0.01	0.686	0.206	-0.046
0917+3152	1237661382232768711	20.42 ± 0.02	-21.57 ± 0.02	0.057 ± 0.001	0.237 ± 0.004	0.108 ± 0.002	0.452 ± 0.007	0.121 ± 0.005	0.542 ± 0.023	8.00 ± 0.45	0.88 ± 0.02	0.783	0.143	-0.111
0925+1403 ^f	1237671262812897597	20.96 ± 0.01	-20.90 ± 0.01	0.058 ± 0.001	0.245 ± 0.002	0.122 ± 0.001	0.514 ± 0.005	0.121 ± 0.004	0.539 ± 0.019	8.00 ± 0.33	0.89 ± 0.02	0.555	0.225	-0.112
0926+4428	1237657630590107652	19.91 ± 0.03	-20.12 ± 0.03	0.137 ± 0.003	0.343 ± 0.009	0.263 ± 0.006	0.660 ± 0.018	0.155 ± 0.002	0.472 ± 0.004	4.09 ± 0.09	0.68 ± 0.01	0.292	0.132	0.099
0927+1740	1237667536393142625	20.88 ± 0.02	-21.03 ± 0.02	0.149 ± 0.003	0.582 ± 0.011	0.322 ± 0.006	1.256 ± 0.024	0.421 ± 0.036	1.824 ± 0.139	4.84 ± 0.26	0.81 ± 0.02	0.742	0.220	-0.090
1009+2916	1237665126921011548	21.18 ± 0.03	-19.17 ± 0.03	0.078 ± 0.002	0.245 ± 0.006	0.150 ± 0.003	0.474 ± 0.011	0.222 ± 0.026	0.794 ± 0.083	8.00 ± 0.61	0.78 ± 0.03	0	0.163	0.024
1018+4106	1237661851459584247	20.90 ± 0.02	-19.95 ± 0.02	0.164 ± 0.003	0.546 ± 0.011	0.276 ± 0.005	0.923 ± 0.018	0.326 ± 0.037	1.224 ± 0.122	7.42 ± 0.49	0.79 ± 0.03	0.380	0.099	-0.002
1025+3622	1237664668435677291	18.83 ± 0.01	-20.25 ± 0.01	0.400 ± 0.003	0.627 ± 0.007	0.878 ± 0.007	1.376 ± 0.015	0.257 ± 0.008	0.582 ± 0.013	4.82 ± 0.09	0.48 ± 0.01	0.338	0.082	0.201
1032+2717	1237667211592794251	20.89 ± 0.02	-19.43 ± 0.02	0.120 ± 0.002	0.368 ± 0.007	0.261 ± 0.005	0.802 ± 0.015	0.371 ± 0.028	1.189 ± 0.085	5.51 ± 0.28	0.92 ± 0.02	0.384	0.150	0.077
1054+5238	1237658801495474207	19.65 ± 0.01	-21.30 ± 0.01	0.100 ± 0.001	0.381 ± 0.004	0.204 ± 0.002	0.775 ± 0.008	0.126 ± 0.002	0.497 ± 0.008	5.90 ± 0.14	0.93 ± 0.01	0.280	0.107	-0.029
1122+6154	1237655464839479591	21.29 ± 0.03	-19.23 ± 0.03	0.036 ± 0.001	0.120 ± 0.003	0.082 ± 0.002	0.276 ± 0.006	0.174 ± 0.015	0.583 ± 0.051	8.00 ± 0.61	1.00 ± 0.03	0.514	0.058	0.056
1133+6514	1237651067351073064	20.35 ± 0.01	-20.31 ± 0.01	0.140 ± 0.001	0.458 ± 0.005	0.260 ± 0.002	0.852 ± 0.008	0.272 ± 0.008	1.035 ± 0.028	4.55 ± 0.10	0.74 ± 0.01	0.162	0.079	-0.010
1137+3524	1237665129613885585	19.59 ± 0.01	-20.52 ± 0.01	0.168 ± 0.002	0.376 ± 0.005	0.365 ± 0.003	0.817 ± 0.010	0.155 ± 0.004	0.502 ± 0.008	4.25 ± 0.07	0.48 ± 0.00	0.171	0.132	0.074
1152+3400 ^f	1237665127467647162	20.79 ± 0.02	-21.30 ± 0.02	0.061 ± 0.001	0.265 ± 0.003	0.119 ± 0.002	0.513 ± 0.006	0.106 ± 0.003	0.515 ± 0.013	6.73 ± 0.26	0.79 ± 0.02	0.480	0.143	-0.179
1205+2620	1237667321644908846	21.29 ± 0.03	-21.06 ± 0.03	0.079 ± 0.002	0.309 ± 0.008	0.175 ± 0.004	0.682 ± 0.018	0.129 ± 0.009	0.628 ± 0.034	5.45 ± 0.30	0.64 ± 0.02	0.750	0.138	-0.180
1219+1526	1237661070336852109	20.18 ± 0.01	-19.84 ± 0.01	0.071 ± 0.007	0.223 ± 0.003	0.159 ± 0.002	0.496 ± 0.005	0.073 ± 0.001	0.238 ± 0.004	7.01 ± 0.20	0.93 ± 0.01	0	0.190	0.072
1244+0216	1237671266571387104	19.95 ± 0.01	-20.88 ± 0.01	0.258 ± 0.002	0.824 ± 0.007	0.492 ± 0.004	1.570 ± 0.012	0.270 ± 0.005	1.021 ± 0.016	2.99 ± 0.04	0.71 ± 0.01	0.251	0.179	-0.006
1249+1234	1237661817096962164	20.73 ± 0.01	-20.51 ± 0.01	0.104 ± 0.008	0.358 ± 0.004	0.212 ± 0.002	0.726 ± 0.007	0.223 ± 0.008	0.906 ± 0.028	5.95 ± 0.15	0.71 ± 0.01	0.343	0.217	-0.048
1333+6246 ^f	1237651249891967264	21.16 ± 0.01	-20.22 ± 0.01	0.076 ± 0.001	0.326 ± 0.003	0.193 ± 0.002	0.830 ± 0.008	0.151 ± 0.005	0.702 ± 0.023	6.21 ± 0.20	0.86 ± 0.01	0	0.140	-0.140
1339+1516	1237664292084318332	20.86 ± 0.03	-19.59 ± 0.03	0.052 ± 0.001	0.160 ± 0.004	0.109 ± 0.003	0.332 ± 0.008	0.143 ± 0.007	0.458 ± 0.022	8.00 ± 0.43	0.91 ± 0.02	0.452	0.219	0.078
1424+4217	1237661360765730849	20.32 ± 0.02	-19.54 ± 0.02	0.097 ± 0.002	0.266 ± 0.004	0.230 ± 0.003	0.630 ± 0.009	0.137 ± 0.005	0.424 ± 0.013	8.00 ± 0.28	0.78 ± 0.01	0.111	0.074	0.091
1428+1653	1237668297680683015	19.33 ± 0.01	-21.13 ± 0.01	0.150 ± 0.002	0.400 ± 0.004	0.321 ± 0.003	0.856 ± 0.009	0.199 ± 0.004	0.608 ± 0.011	3.95 ± 0.07	0.76 ± 0.01	0.690	0.142	0.097
1429+0643	1237662268069511204	19.49 ± 0.02	-20.40 ± 0.02	0.119 ± 0.002	0.307 ± 0.005	0.234 ± 0.003	0.606 ± 0.009	0.124 ± 0.002	0.365 ± 0.004	7.09 ± 0.13	0.77 ± 0.01	0.208	0.183	0.112
1440+4619	1237662301362978958	20.13 ± 0.02	-21.66 ± 0.02	0.091 ± 0.002	0.348 ± 0.006	0.207 ± 0.003	0.795 ± 0.014	0.147 ± 0.006	0.655 ± 0.023	8.00 ± 0.30	0.74 ± 0.01	0.613	0.103	-0.111
1442-0209 ^f	1237655498671849789	21.04 ± 0.01	-20.74 ± 0.01	0.055 ± 0.001	0.215 ± 0.002	0.123 ± 0.007	0.485 ± 0.003	0.093 ± 0.003	0.408 ± 0.011	8.00 ± 0.34	0.81 ± 0.02	0.388	0.392	-0.099

Table 1
(Continued)

Green Pea ID ^a	SDSS ObjID ^b	$m_{\text{UV}}^{\text{c,d}}$ (mag)	$M_{\text{UV}}^{\text{c,d}}$ (mag)	$r_{\text{cir},50}^{\text{f,g}}$ (arcsec)	$r_{\text{cir},50}^{\text{h,g}}$ (kpc)	$r_{\text{cir,p}}^{\text{i,g}}$ (arcsec)	$r_{\text{cir,p}}^{\text{j,g}}$ (kpc)	$r_{\text{cir,eff}}^{\text{k}}$ (arcsec)	$r_{\text{cir,eff}}^{\text{l}}$ (kpc)	n^{m}	b/a^{n}	$A_{\text{int}}^{\text{o}}$ (mag)	A_{MW}^{p} (mag)	k^{q} (mag)
1454+4528	1237662301900964026	20.87 ± 0.02	−20.86 ± 0.02	0.058 ± 0.001	0.219 ± 0.005	0.150 ± 0.003	0.567 ± 0.012	0.117 ± 0.006	0.480 ± 0.024	8.00 ± 0.51	0.84 ± 0.03	0.691	0.303	−0.057
1457+2232	1237665549967294628	20.61 ± 0.01	−19.06 ± 0.01	0.075 ± 0.001	0.193 ± 0.002	0.163 ± 0.002	0.420 ± 0.004	0.240 ± 0.009	0.622 ± 0.024	8.00 ± 0.23	0.99 ± 0.01	0.237	0.347	0.159
1503+3644 ^r	1237661872417407304	21.27 ± 0.01	−20.46 ± 0.01	0.056 ± 0.001	0.250 ± 0.003	0.109 ± 0.001	0.485 ± 0.006	0.132 ± 0.006	0.660 ± 0.026	8.00 ± 0.33	0.80 ± 0.02	0.031	0.111	−0.201
1514+3852	1237661362380734819	21.02 ± 0.02	−20.52 ± 0.02	0.049 ± 0.001	0.191 ± 0.005	0.119 ± 0.003	0.466 ± 0.011	0.133 ± 0.009	0.637 ± 0.037	8.00 ± 0.50	0.67 ± 0.02	0	0.157	−0.164
1543+3446	1237662336790036887	21.21 ± 0.02	−18.72 ± 0.02	0.191 ± 0.004	0.475 ± 0.012	0.337 ± 0.007	0.839 ± 0.021	0.345 ± 0.039	1.081 ± 0.097	5.35 ± 0.33	0.63 ± 0.02	0	0.214	0.087
1559+0841	1237662636912280219	21.69 ± 0.03	−19.63 ± 0.03	0.050 ± 0.002	0.209 ± 0.006	0.096 ± 0.003	0.397 ± 0.011	0.128 ± 0.016	0.568 ± 0.064	8.00 ± 0.95	0.88 ± 0.05	0	0.282	−0.105
2237+1336	1237656495641788638	20.18 ± 0.02	−21.76 ± 0.02	0.222 ± 0.003	0.966 ± 0.013	0.453 ± 0.006	1.966 ± 0.025	0.608 ± 0.058	2.669 ± 0.251	6.42 ± 0.35	0.98 ± 0.02	0.521	0.418	−0.099

Notes.

^a GP IDs match those in Y17.

^b SDSS DR14 BestObjID.

^c The measured apparent UV magnitude.

^d The associated errors are magnitude measurement uncertainties based on photon counting statistics (i.e., Poisson statistics) and propagation of the errors during the image calibration procedures such as flat-field correction.

^e The extinction and k -corrected absolute UV magnitude at 1877 Å.

^f The circularized Petrosian half-light radius in units of arcseconds.

^g The associated errors are based on the associated flux measurement uncertainties.

^h The circularized Petrosian half-light radius in the units of kiloparsecs assuming the adopted cosmological parameters in Section 1.

ⁱ The circularized Petrosian radius in units of arcseconds.

^j The circularized Petrosian radius in units of kiloparsecs assuming the adopted cosmological parameters in Section 1.

^k The circularized effective radius and the associated uncertainties in units of arcseconds derived from the GALFIT surface brightness fitting in Section 2.2.

^l The circularized effective radius in units of kiloparsecs assuming the adopted cosmological parameters in Section 1.

^m The Sérsic index and the associated uncertainties derived from the GALFIT surface brightness fitting in Section 2.2.

ⁿ The apparent axis ratio and the associated uncertainties derived from the GALFIT surface brightness fitting in Section 2.2.

^o The internal extinction correction derived in Paper I based on the Balmer decrement. Zero indicates that the observed ratio of $H\alpha/H\beta$ is smaller than 2.86. See their Section 2.3 and also Section 2.2 of Y17 for details.

^p The Milky Way extinction correction derived in Paper I based on the NASA/IPAC Galactic Dust Reddening and Extinction tool. See their Section 2.3 for details.

^q The k -correction derived in Paper I at 1877 Å assuming the UV slope of -2 . See their Section 2.3 for details.

^r Confirmed Lyman-continuum leakers identified by Izotov et al. (2016).

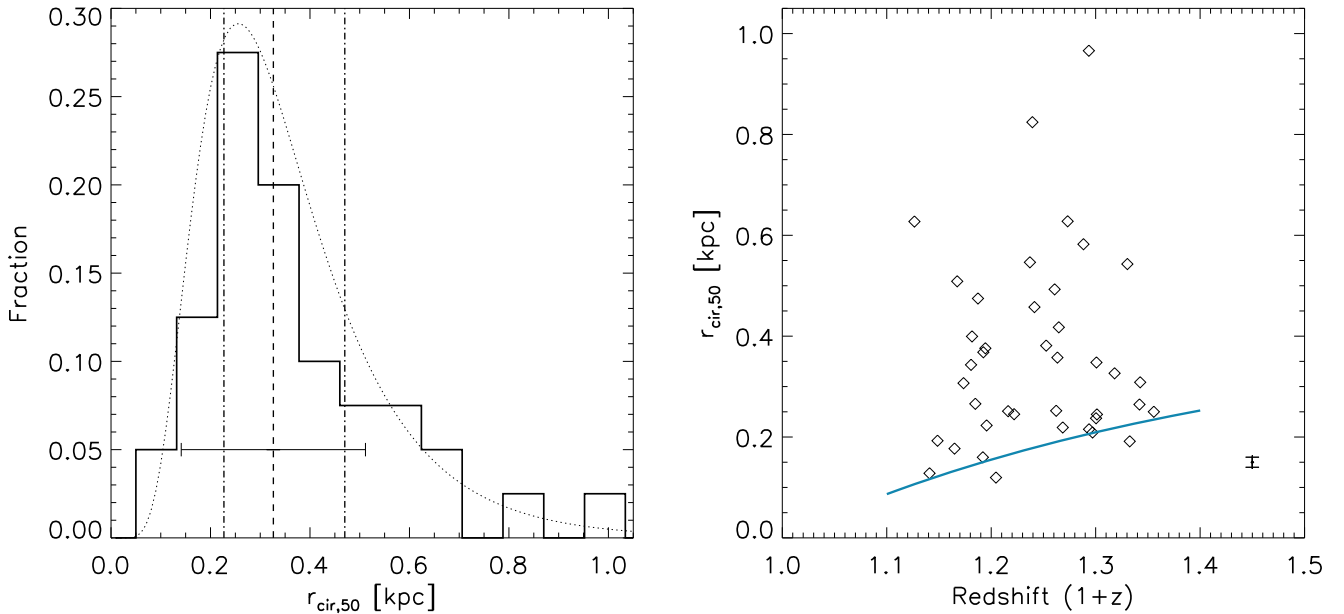


Figure 1. Left: the size ($r_{\text{cir},50}$) distribution of 40 sample GP galaxies. The vertical dashed line indicates the median $r_{\text{cir},50}$ of 0.33 kpc, while the horizontal solid line indicates a 1σ of 0.19 kpc. The 25th and 75th percentiles of the size distribution are 0.23 kpc and 0.47 kpc, respectively, marked as the vertical dotted-dashed lines. The semi-interquartile range of the distribution is 0.12 kpc. The dotted curve shows the log-normal fit to the size distribution. This fit has a median size (r_{med}) of 0.32 kpc and a width ($\sigma_{\ln(r_{\text{cir},50})}$) of 0.48. The fitted log-normal probability density function is scaled by a factor of 0.1 to visualize with the actual distribution. Right: the size vs. redshift of GPs. The blue solid line shows the typical PSF FWHM of COS/NUV images in units of physical kiloparsecs. The panel shows that the sizes of sample GPs are mostly resolved with the NUV images. The typical measurement error in $r_{\text{cir},50}$ is marked in the bottom right.

models (e.g., Peebles 1969; Fall & Efstathiou 1980; Barnes & Efstathiou 1987; Mo et al. 1998) where the pre-collapse dark matter halo angular momentum is predicted to have a log-normal distribution. The associated dimensionless spin parameter $\lambda \equiv \frac{J|E|^{1/2}}{GM^{5/2}}$ —where J , E , M , and G indicate the total angular momentum, energy, and mass of the system, and the gravitational constant, respectively—follows the log-normal distribution with the associated peak value $\lambda_{\text{med}} \sim 0.05$ and width $\sigma_{\ln(\lambda)} \sim 0.5$ – 0.6 (Barnes & Efstathiou 1987; Warren et al. 1992; Cole & Lacey 1996; Davis & Natarajan 2009). Assuming that the baryonic component acquired most of its angular momentum through its surrounding dark matter halos and that the galaxy disk size is largely determined by the multiplication of λ by the virial radius (R_{vir} ; e.g., Fall & Efstathiou 1980; Mo et al. 1998), it seems reasonable to expect that the galaxy disk size distribution also follows a log-normal distribution, reflecting the underlying dark matter halo properties. Our fitted log-normal UV size distribution of sample GPs with the associated $\sigma_{\ln(r_{\text{cir},50})}$ of 0.47 shows a $\sim 6\%$ narrower width compared to the predicted dark matter halo λ distribution with the associated $\sigma_{\ln(\lambda)}$ of ~ 0.5 , but is broadly consistent with other types of SFGs at low and high redshifts (e.g., de Jong & Lacey 2000; Shen et al. 2003; Huang et al. 2013).

3.2. UV Size–Luminosity Relation of GPs

The size–luminosity relationship for galaxies is a key piece to understand the growth history of galaxies over cosmic time. For the high- z universe, the UV size–luminosity relations of SFGs such as LAEs and UV continuum-selected Lyman-break galaxies (LBGs) have been previously investigated (e.g., Oesch et al. 2010; Huang et al. 2013; Jiang et al. 2013; Ono et al. 2013; Holwerda et al. 2015, 2020; Shibuya et al. 2015; Bridge et al. 2019). The size–luminosity relation is often parameterized

as a power law with a slope of α :

$$r_{\text{cir},50} = r_0 \left(\frac{L_{\text{UV}}}{L_0} \right)^\alpha, \quad (2)$$

where L_{UV} , L_0 , and r_0 are the UV luminosity of galaxies, a fiducial UV luminosity (which we take as the same redshift 3 characteristic luminosity we used in Section 2.2, i.e., $L_0 = L_{*,z=3}$, corresponding to $M_{\text{UV}} = -21$), and the size at L_0 , respectively.

The fitted α and r_0 of our sample GPs are 0.30 ± 0.09 and 0.38 ± 0.03 kpc, respectively. The slope value is consistent within the uncertainties with those for high- z ($2 \lesssim z \lesssim 8$) star-forming galaxy populations, which show a slope range of $0.15 \lesssim \alpha \lesssim 0.5$ with the typical α of ~ 0.27 (Grazian et al. 2012; Huang et al. 2013; Jiang et al. 2013; Shibuya et al. 2015; Curtis-Lake et al. 2016). A brief interpretation of the slope of the size–luminosity relation might come from theoretical galaxy disk formation models (as in Section 3.1). Based on the Tully–Fisher relation and the assumed constant mass-to-light (M/L) ratio of disks, the fiducial slope of the size–luminosity derived is $1/3$ (Mo et al. 1998). The deviation from the fiducial slope value could be due to varying M/L ratio and/or stellar feedback such as supernova (SN) feedback from star formation in disks, as such effects can change the slope value (Wyithe & Loeb 2011; Liu et al. 2017). The fitted slope of our sample GPs is broadly in agreement within the uncertainties with the suggested value of 0.25 from the semianalytic model that accounts for the effect of SN feedback (Liu et al. 2017).

Figure 2 shows the UV size–luminosity relation of our sample GPs. Comparing the distribution of individual data points to lines of constant effective star formation intensity (S_{eff}) demonstrates that all of our sample GPs have $S_{\text{eff}} \gtrsim 1 M_\odot \text{ yr}^{-1} \text{ kpc}^{-2}$, which is 2+ orders of magnitude above those of typical SFGs ($\lesssim 0.01 M_\odot \text{ yr}^{-1} \text{ kpc}^{-2}$) (e.g., Kennicutt 1998). This is mainly

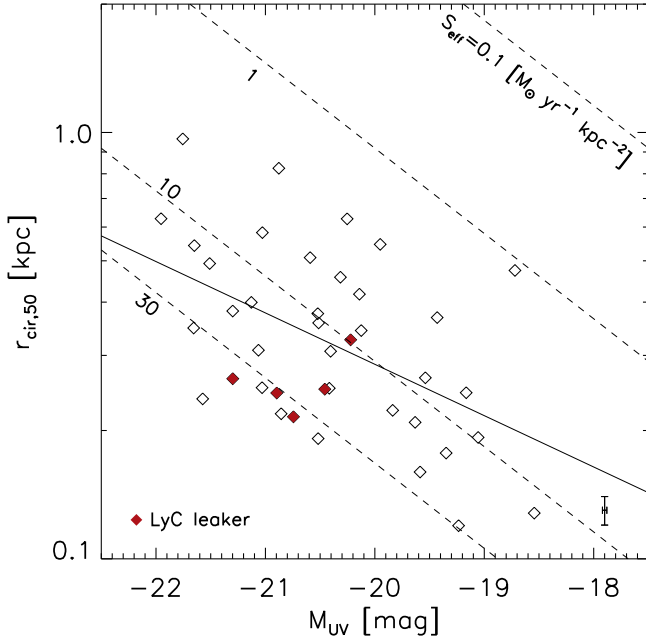


Figure 2. The UV-continuum size vs. luminosity relation of GPs. The solid line shows the linear fit to the UV size–luminosity relation (i.e., Equation (2)), with the best-fit slope α of 0.30 ± 0.09 and the intercept r_0 of 0.38 ± 0.03 kpc at $M_{UV} = -21$. The dashed lines indicate a constant effective SFI (equivalent to star formation rate surface density) defined in Section 3.2. The comparison of individual data points with the constant effective SFI lines shows that GPs have SFI that is relatively high (by at least 2 orders of magnitude) compared to typical SFGs. (GPs have $S_{\text{eff}} \gtrsim 1 M_{\odot} \text{ yr}^{-1} \text{ kpc}^{-2}$ vs. $\sim 0.01 M_{\odot} \text{ yr}^{-1} \text{ kpc}^{-2}$ for typical low-redshift SFGs). The typical measurement errors of 0.01 kpc and 0.02 mag in $r_{\text{cir},50}$ and UV magnitude are marked in the bottom right. The red-filled diamonds are the five confirmed LyC leakers from Izotov et al. (2016).

due to the compact sizes of GPs given their UV luminosity. Here, the effective SFI is defined as $S_{\text{eff}} \equiv \frac{\text{SFR}}{2\pi r_{\text{cir},50}^2} \left(\frac{M_{\odot} \text{ yr}^{-1}}{\text{kpc}^2} \right)$. To convert the measured UV luminosity to the corresponding SFR, we adopt the solar bolometric magnitude of 4.74 (Bessell et al. 1998), and the UV to bolometric luminosity (L_{bol}) ratio ($L_{\text{UV}}/L_{\text{bol}}$) of 0.33 and the scale factor $L_{\text{bol}}/(4.5 \times 10^9 L_{\odot}) = \text{SFR}/(1 M_{\odot} \text{ yr}^{-1})$ that are derived from the starburst population modeling by Meurer et al. (1997). The starburst population modeling assumes a solar metallicity and the Salpeter initial mass function (Salpeter 1955) with lower and upper mass limits of $0.1 M_{\odot}$ and $100 M_{\odot}$, respectively.

The effective SFI of our sample GPs mostly ranges from 1 to $\sim 30 M_{\odot} \text{ yr}^{-1} \text{ kpc}^{-2}$ as shown in the figure. The range of the effective SFI is similar to the central 250 pc region SFI ($S_{250 \text{ pc}}$) that we reported in Paper I, which ranges from 2.3 to $46 M_{\odot} \text{ yr}^{-1} \text{ kpc}^{-2}$ with a mean $S_{250 \text{ pc}}$ of $15 M_{\odot} \text{ yr}^{-1} \text{ kpc}^{-2}$ for the same sample GPs. This is not unexpected, since the typical $r_{\text{cir},50}$ of our sample GPs is ~ 0.3 kpc (i.e., Figure 1), so that the effective SFI is measured in a region that largely overlaps the central 250 pc for most sample objects.

3.3. Correlations between UV Size and the Ly α Properties of GPs

In this section, we investigate the possible correlations between UV size and the Ly α properties such as $\text{EW}(\text{Ly}\alpha)$, $f_{\text{esc}}^{\text{Ly}\alpha}$, and $L(\text{Ly}\alpha)$ in our sample GPs. Figure 3 shows the correlations between $r_{\text{cir},50}$ and $\text{EW}(\text{Ly}\alpha)$, $f_{\text{esc}}^{\text{Ly}\alpha}$, and $L(\text{Ly}\alpha)$. Panel (a) shows the correlation between $r_{\text{cir},50}$ and $\text{EW}(\text{Ly}\alpha)$.

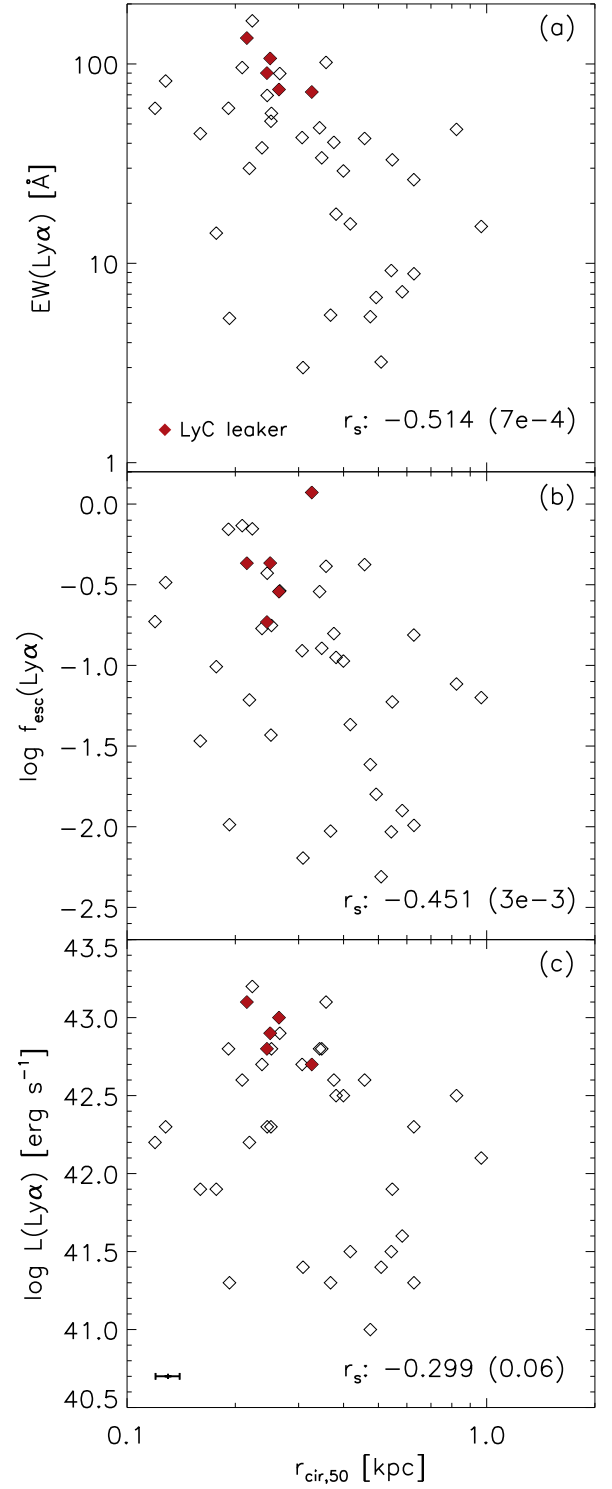


Figure 3. The correlations between $r_{\text{cir},50}$ vs. $\text{EW}(\text{Ly}\alpha)$ (panel (a)), $f_{\text{esc}}^{\text{Ly}\alpha}$ (panel (b)), and $L(\text{Ly}\alpha)$ (panel (c)). The format is the same as in Figure 2. The associated Spearman correlation coefficient r_s values (p -values) are shown in the bottom right of each panel. Note that the presented Ly α properties (i.e., $\text{EW}(\text{Ly}\alpha)$, $f_{\text{esc}}^{\text{Ly}\alpha}$, and $L(\text{Ly}\alpha)$) largely show anticorrelations with $r_{\text{cir},50}$ in our sample GPs, suggesting that small sizes are preferred for significant Ly α emission. The horizontal error bar in panel (c) indicates the typical measurement uncertainties in $r_{\text{cir},50}$. The typical measurement uncertainties of the adopted $\text{EW}(\text{Ly}\alpha)$, $f_{\text{esc}}^{\text{Ly}\alpha}$, and $L(\text{Ly}\alpha)$ from Y17 are $\sim 15\%$ mainly dominated by the systematic error.

Based on the distribution and the associated Spearman correlation coefficient (hereafter, r_s) (p -value) of -0.514 (7×10^{-4}), there is a statistically significant anticorrelation

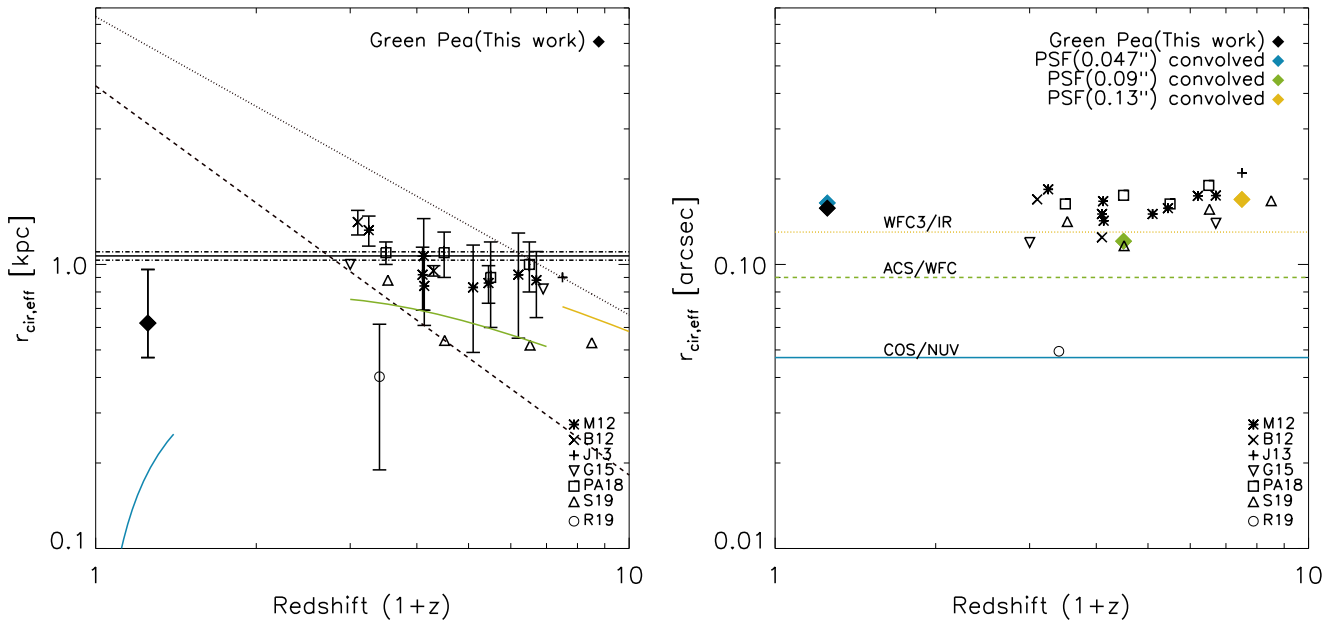


Figure 4. Left: the median UV-continuum size (as measured by $r_{\text{cir,eff}}$ in the same way at all redshifts) of sample GPs (the filled diamond at $1+z \sim 1.25$) compared to those of high- z LAEs. The sizes of high- z LAEs are from the literature (asterisk: Malhotra et al. 2012; M12, x mark: Bond et al. 2012; B12, cross: Jiang et al. 2013; J13, downward triangle: Guaita et al. 2015; G15, square: Paulino-Afonso et al. 2018; PA18, triangle: Shibuya et al. 2019; S19, and circle: Ritondale et al. 2012; R19). The associated error bar indicates the 1σ standard deviation of size distribution of respective sample galaxies except for that of sample GPs and of R19, which show the associated interquartile range and the uncertainties derived from random MCMC realizations to quantify errors of their size measurements of lensed LAEs. The data points for B12 for the $1+z=4.1$ sample LAEs and for G15 for the $1+z=3.1$ sample LAEs are shifted by 0.2 in x -axis for clarity. The solid horizontal line is the weighted mean size of the combined sample LAEs of M12 and PA18, and the dotted-dashed lines are the associated weighted standard deviation of the weighted mean size. The colored solid lines are the physical sizes corresponding to the typical PSF FWHM of different instruments that are marked within their relevant redshift range for LAE size measurements as indicated in the right panel. The dashed line is the predicted size evolution of LAEs based on S19. The dotted line is the predicted size evolution of LBGs from Bouwens et al. (2004). Our sample GPs do not follow either of these predicted size evolution models. The small median size of sample GPs does not change significantly even if the sample GPs are divided into specific L_{UV} and $\text{EW}(\text{Ly}\alpha)$ bins as listed in Table 2. See the text for further details. Right: same as the left panel, but for the corresponding angular sizes of GPs and high- z LAEs that are PSF-convolved in quadrature, except for the sizes of lensed LAEs (R19, circle) and of LAEs from B12 and G15. The typical PSF FWHM of different HST instrument filters are marked as the colored horizontal lines. The blue, green, and orange diamonds are the PSF-convolved angular sizes of original median physical size of sample GPs (black diamond) by employing the different PSF FWHM indicated by each corresponding color. Note that the PSF-convolved median sizes of sample GPs and high- z LAEs become undersampled as we go to higher redshift. See the text for further details. The non-evolving size of GPs suggests that a small size is crucial for a galaxy to become a $\text{Ly}\alpha$ -emitter.

between the two parameters such that a smaller UV size is preferred for a larger $\text{EW}(\text{Ly}\alpha)$.

A similar anticorrelation with the associated r_s (p -value) of -0.64 (0.03) was reported based on 12 local SFGs ($0.03 < z < 0.2$) from the $\text{Ly}\alpha$ reference sample (LARS) (Guaita et al. 2015). For high- z LAEs at $z \simeq 2.1$ and 3.1 , there is a systematic trend seen such that high $\text{EW}(\text{Ly}\alpha)$ sample LAEs have a smaller median UV size compared to that of low $\text{EW}(\text{Ly}\alpha)$ sample LAEs (i.e., Bond et al. 2012). Also, a linear fit to the UV size and $\text{EW}(\text{Ly}\alpha)$ relation for a sample of high- z LAEs at $2 \lesssim z \lesssim 6$ showing a negative slope of -3.5 by Paulino-Afonso et al. (2018) seems qualitatively consistent with the anticorrelation shown in our sample GPs.

A correlation between $r_{\text{cir},50}$ and $f_{\text{esc}}^{\text{Ly}\alpha}$ is shown in panel (b), which shows a qualitatively similar anticorrelation to that in panel (a). The associated r_s (p -value) is -0.451 (3×10^{-3}). The distribution and the associated r_s seem to suggest that a smaller UV size is preferred for larger $f_{\text{esc}}^{\text{Ly}\alpha}$. The same correlation was investigated based on the 12 LARS sample galaxies, although their r_s (p -value) of -0.22 (0.48) is not statistically significant (Guaita et al. 2015).

Panel (c) shows the correlation between $r_{\text{cir},50}$ and $L(\text{Ly}\alpha)$. First, we note that one galaxy (GP ID 0339-0725) is omitted from this panel only, since it has no reported $L(\text{Ly}\alpha)$ in Y17. Compared to the other correlations examined above with $\text{EW}(\text{Ly}\alpha)$ and $f_{\text{esc}}^{\text{Ly}\alpha}$, $L(\text{Ly}\alpha)$ does not show a statistically significant anticorrelation with $r_{\text{cir},50}$, as the associated r_s (p -value) is only -0.299 (0.06). Nonetheless, it also seems evident that the large UV size is

not preferred for high $L(\text{Ly}\alpha)$, as a previous study (Paulino-Afonso et al. 2018) also shows a negative slope -0.51 of the linear fit to the UV size and $L(\text{Ly}\alpha)$ relation based on a sample of high- z LAEs.

The five confirmed LyC leakers in our sample GPs are marked as the red diamonds in Figure 3. Due to their high values of $\text{EW}(\text{Ly}\alpha)$, $f_{\text{esc}}^{\text{Ly}\alpha}$, and $L(\text{Ly}\alpha)$ (Y17), and relatively small $r_{\text{cir},50}$ compared to the sizes of the entire sample GPs, the confirmed LyC leakers occupy the top left of each panel (that is, small $r_{\text{cir},50}$ and large $\text{EW}(\text{Ly}\alpha)$ (panel (a)), $f_{\text{esc}}^{\text{Ly}\alpha}$ (panel (b)), and $L(\text{Ly}\alpha)$ (panel (c)), respectively).

3.4. The Size of GPs Compared to High- z LAEs

Malhotra et al. (2012) show that the sizes of $\text{Ly}\alpha$ galaxies are similar at all redshifts, so GPs should have similar sizes to high- z galaxies. Shibuya et al. (2019), however, argue that the sizes of $\text{Ly}\alpha$ galaxies evolve with redshift as $r_{\text{cir,eff}} \propto (1+z)^\beta$ with (β) values of -1.37 , similar to those of LBGs. At the redshift of GPs ($z = 0.1$ – 0.3) these predictions differ by a factor of 10. But the typical size (i.e., the median $r_{\text{cir,eff}}$) of $\text{Ly}\alpha$ galaxies seems to decrease by a factor of 1.6 instead of increasing by a factor of 10 from $z > 2$ to $z \simeq 0.3$.

The left panel of Figure 4 shows the compilation of the median physical sizes of our sample GPs and high- z LAEs as a function of redshift. For the sizes of high- z LAEs at $2 \lesssim z \lesssim 7$, we refer to previous studies (i.e., Malhotra et al. 2012;

Table 2
The Representative UV Size ($r_{\text{cir,eff}}$) of GP Subsamples with Different L_{UV} and $\text{EW}(\text{Ly}\alpha)$ Criteria

$L_{\text{UV}}/L_{*,z=3}$	N	Mean (No $\text{EW}(\text{Ly}\alpha)$ Cut)	Median	N	Mean ($\text{EW}(\text{Ly}\alpha) > 20 \text{ \AA}$)	Median
0.1–0.3	10	0.68	$0.60^{+0.19}_{-0.09} \text{ kpc}^a$	6	0.56	$0.57^{+0.02}_{-0.11} \text{ kpc}^a$
0.3–1	18	0.71	$0.64^{+0.36}_{-0.16} \text{ kpc}^a$	16	0.67	$0.64^{+0.27}_{-0.16} \text{ kpc}^a$
1–2.4	12	1.01	$0.65^{+0.63}_{-0.10} \text{ kpc}^a$	5	0.57	$0.55^{+0.06}_{-0.01} \text{ kpc}^a$
0.1–2.4	40	0.79	$0.62^{+0.34}_{-0.15} \text{ kpc}^a$	27	0.63	$0.57^{+0.13}_{-0.09} \text{ kpc}^a$

Note.

^a The plus and minus values indicate the 75th and 25th percentiles from the median size, respectively.

Bond et al. 2012; Jiang et al. 2013; Guaita et al. 2015; Paulino-Afonso et al. 2018; Ritondale et al. 2019; Shibuya et al. 2019). The sizes from Guaita et al. (2015) are based on their simulated images, which were produced by taking low-redshift LARS-LAE galaxies and simulating the effects of dimming due to redshift and observational effects at $z \sim 2$ and 5.7, respectively. The median size of our sample GPs (i.e., the filled diamond) does not follow the predicted size growth evolution of either LAEs (i.e., the dashed line) or LBGs (i.e., the dotted line) as suggested by previous studies (i.e., Bouwens et al. 2004 for LBGs and Shibuya et al. 2019 for LAEs)—the plotted size evolution curves of LAEs and LBGs in the figure show the reported power-law fitting slope (β) values of -1.37 ± 0.65 and -1.05 ± 0.21 in the relation of $r_{\text{cir,eff}} \propto (1+z)^\beta$ for high- z LAEs and LBGs, respectively. Also, to derive the intercept of each size evolution curve we use the reported size at $z \sim 3.5$ (for LAEs) and at $z \sim 5$ (for LBGs), respectively, from the previous studies (see Figure 9 of Shibuya et al. 2019 for LAEs and Figure 4 of Bouwens et al. 2004 for LBGs for details).

In particular, the median size (i.e., the median effective radius $r_{\text{cir,eff}}$) of 0.62 kpc of our sample GPs is approximately a factor of 7 smaller than predicted using the LAE size evolution models from Shibuya et al. (2019). Our size measurement uncertainties are typically ~ 0.03 kpc and cannot explain the discrepancy. This size difference does not change significantly even if we divided our sample GPs depending on the specific L_{UV} and/or $\text{EW}(\text{Ly}\alpha)$ bins similar to previous studies for the size of LAEs. For example, a subset of our sample with luminosities $0.3 < L/L_{*,z=3} < 1$ and $\text{EW}(\text{Ly}\alpha) > 20 \text{ \AA}$ contains 16 GPs whose median size is $0.64^{+0.27}_{-0.16} \text{ kpc}$, indistinguishable from the result for our full sample. The mean and median sizes of our GP subsamples with various different L_{UV} and $\text{EW}(\text{Ly}\alpha)$ cuts are listed in Table 2.

On average GPs show radii that are a factor of ~ 1.6 smaller compared to high- z LAEs (i.e., 0.62 kpc versus ~ 1 kpc). This difference is due to both the angular resolution of the HST instruments, which would increase as $(1+z)$ for the same rest wavelength, and also due to the angular diameter distance increase with redshift. The spatial resolution for different instruments is shown in the right panel of Figure 4. If we assume that the sizes of LAEs is unchanged with redshift and convolve the median GPs radius of 0.62 kpc with the typical PSF FWHM of $0''.09$ of ACS/WFC instrument or the typical PSF FWHM of $0''.13$ of WFC3/IR, the measured radii of high- z LAEs are consistent with the radii of GPs. In the right panel of Figure 4 we show the results of convolving measured median angular size of GPs (black diamond) with three different PSF FWHM of different instruments (that is, COS/NUV (blue diamond), ACS/WFC (green diamond), and

WFC3/IR (orange diamond)) to show the effects of different PSF FWHM on the measured size of galaxies. Moreover, the PSF-convolved median sizes of GPs and high- z LAEs with ACS and WFC3 instruments in the unit of pixels show ~ 7.1 pixels, ~ 2.4 pixels, and ~ 1.3 pixels, respectively. This suggests that the measured median sizes of galaxies become getting undersampled as we go to higher redshift.

This result is supported by measurements of the UV continuum size for lensed LAEs at $z=2-3$ by Ritondale et al. (2019), who find $r_{\text{maj}} = 0.561^{+0.013}_{-0.110} \text{ kpc}$, with the corresponding circularized size of $0.403 \pm 0.213 \text{ kpc}$ (the open circle in the left panel of Figure 4). This measurement is ~ 2.5 times smaller than the sizes measured for non-lensed LAEs at similar redshifts, and broadly comparable to the sizes of GPs, suggesting again that spatial resolution limits size measurements for high-redshift LAEs.

4. Summary and Conclusions

In this study, we have measured the UV-continuum size and luminosity of a sample of 40 GPs. As GPs are the best local analogs to high- z LAEs, their physical proximity and the high spatial resolution of COS/NUV images (PSF FWHM of 0.047 arcsec with high sampling of $0.0235 \text{ arcsec pixel}^{-1}$) have enabled us to study the spatially resolved UV size and luminosity properties of LAEs in local universe and compare with those of high- z LAEs in detail. The main results are summarized as follows.

1. GPs show compact sizes with a median $r_{\text{cir},50}$ of 0.33 kpc. The size distribution (Figure 1) is narrow (with its semi-interquartile range of 0.12 kpc) and is well fitted by a log-normal distribution with the associated width $\sigma_{\ln(r_{\text{cir},50})}$ of 0.47. While the log-normal shape of the size distribution of GPs is largely consistent with continuum-selected SFGs, the peak ($r_{\text{cir},50}$ at $\simeq 0.3 \text{ kpc}$) of the distribution is smaller due to the compact sizes of GPs.
2. The UV size–luminosity relation of GPs (Figure 2) shows a fitted slope of 0.30 ± 0.09 and an intercept r_0 at $M_{\text{UV}} = -21$ of $0.38 \pm 0.03 \text{ kpc}$. The fitted slope value is consistent with other types of SFGs at low and high redshifts within the uncertainties. ($0.15 \lesssim \alpha \lesssim 0.35$). However, the effective SFI (i.e., star formation rate surface density) of our sample GPs shown in the size–luminosity relation indicates relatively high SFI for GPs ($1-30 M_\odot \text{ yr}^{-1} \text{ kpc}^{-2}$), exceeding the typical SFI of SFGs by 2 orders of magnitude or more.
3. There are anticorrelations between UV-continuum size ($r_{\text{cir},50}$), $\text{EW}(\text{Ly}\alpha)$, $f_{\text{esc}}^{\text{Ly}\alpha}$, and $L(\text{Ly}\alpha)$ in sample GPs (Figure 3). In particular, the anticorrelations between

$r_{\text{cir},50}$, $\text{EW}(\text{Ly}\alpha)$, and $f_{\text{esc}}^{\text{Ly}\alpha}$ are statistically significant, and suggest that small UV-continuum sizes are associated with $\text{Ly}\alpha$ galaxies.

- The size comparison of sample GPs with high- z LAEs (Figure 4) shows that the typical size of GPs (i.e., the median $r_{\text{cir,eff}}$ of 0.62 kpc) is a factor of ~ 1.6 smaller than those of high- z LAEs (≈ 1 kpc) at $2 \lesssim z \lesssim 6$. Also, the compact size of GPs does not seem to follow the predicted size growth with time of either high- z LAEs or LBGs, rather showing a factor of ~ 7 smaller size than the predicted size at low redshifts. The smaller size of our sample GPs compared to those of high- z LAEs, is, however, due to the different spatial resolution between low- z GPs and high- z LAEs (Figure 4). Once the different resolution is properly taken into account, their sizes are consistent with negligible evolution.

All in all, our UV size and luminosity analysis of GP galaxies suggests that a compact /small size is crucial for escape of $\text{Ly}\alpha$ photons, and that LAEs show constant characteristic size independent of their redshift. Also, our study implies that small sizes can help select $\text{Ly}\alpha$ -emitters.

We thank the referee for constructive comments that improved the manuscript. K.J.K. thanks Nathaniel R. Butler, Sanchayeeta Borthakur, and Rolf A. Jansen for helpful discussions. Support for this work was provided by awards HST-GO-14201, HST-GO-15614, and HST-GO-16054 from STScI, which is operated by AURA, Inc. for the National Aeronautics Space Administration (NASA) under contract NAS 5-26555; by NASA through award number NNG16PJ33C to Arizona State University; and through Chandra Award Number GO-20700693 issued by the Chandra X-Ray Center, which is operated by the Smithsonian Astrophysical Observatory for and on behalf of NASA under contract NAS8-03060.

ORCID iDs

Keunho J. Kim  <https://orcid.org/0000-0001-6505-0293>
 Sangeeta Malhotra  <https://orcid.org/0000-0002-9226-5350>
 James E. Rhoads  <https://orcid.org/0000-0002-1501-454X>
 Huan Yang  <https://orcid.org/0000-0003-2260-7420>

References

- Ahn, S.-H., Lee, H.-W., & Lee, H. M. 2003, *MNRAS*, **340**, 863
 Amorín, R. O., Pérez-Montero, E., & Vilchez, J. M. 2010, *ApJ*, **715**, L128
 Baldwin, J. A., Phillips, M. M., & Terlevich, R. 1981, *PASP*, **93**, 5
 Barnes, J., & Efstathiou, G. 1987, *ApJ*, **319**, 575
 Bessell, M. S., Castelli, F., & Plez, B. 1998, *A&A*, **333**, 231
 Bond, N. A., Gawiser, E., Gronwall, C., et al. 2009, *ApJ*, **705**, 639
 Bond, N. A., Gawiser, E., Guaita, L., et al. 2012, *ApJ*, **753**, 95
 Bouwens, R. J., Illingworth, G. D., Blakeslee, J. P., et al. 2004, *ApJL*, **611**, L1
 Bouwens, R. J., Illingworth, G. D., Oesch, P. A., et al. 2015, *ApJ*, **803**, 34
 Bridge, J. S., Holwerda, B. W., Stefanon, M., et al. 2019, *ApJ*, **882**, 42
 Brunker, S. W., Salzer, J. J., Janowiecki, S., Finn, R. A., & Helou, G. 2020, *ApJ*, **898**, 68
 Cardamone, C., Schawinski, K., Sarzi, M., et al. 2009, *MNRAS*, **399**, 1191
 Cen, R. 2020, *ApJL*, **889**, L22
 Clarke, L., Scarlata, C., & Mehta, V. 2021, *ApJL*, **912**, L22
 Cole, S., & Lacey, C. 1996, *MNRAS*, **281**, 716
 Conselice, C. J., Bershad, M. A., & Jangren, A. 2000, *ApJ*, **529**, 886
 Curtis-Lake, E., McLure, R. J., Dunlop, J. S., et al. 2016, *MNRAS*, **457**, 440
 Davis, A. J., & Natarajan, P. 2009, *MNRAS*, **393**, 1498
 de Barros, S., Vanzella, E., Amorín, R., et al. 2016, *A&A*, **585**, A51
 de Jong, R. S., & Lacey, C. 2000, *ApJ*, **545**, 781
 Dow-Hygelund, C. C., Holden, B. P., Bouwens, R. J., et al. 2007, *ApJ*, **660**, 47
 Fall, S. M., & Efstathiou, G. 1980, *MNRAS*, **193**, 189
 Finkelstein, K. D., Finkelstein, S. L., Tilvi, V., et al. 2015a, *ApJ*, **813**, 78
 Finkelstein, S. L., Ryan, R. E., Papovich, C., et al. 2015b, *ApJ*, **810**, 71
 Gawiser, E., Francke, H., Lai, K., et al. 2007, *ApJ*, **671**, 278
 Gazagnes, S., Chisholm, J., Schaerer, D., et al. 2020, *A&A*, **639**, A85
 Graham, A. W., & Driver, S. P. 2005, *PASA*, **22**, 118
 Graham, A. W., Driver, S. P., Petrosian, V., et al. 2005, *AJ*, **130**, 1535
 Grazian, A., Castellano, M., Fontana, A., et al. 2012, *A&A*, **547**, A51
 Guaita, L., Melinder, J., Hayes, M., et al. 2015, *A&A*, **576**, A51
 Henry, A., Scarlata, C., Martin, C. L., et al. 2015, *ApJ*, **809**, 19
 Hogarth, L., Amorín, R., & Vilchez, J. M. 2020, *MNRAS*, **494**, 3541
 Holwerda, B. W., Bouwens, R., Oesch, P., et al. 2015, *ApJ*, **808**, 6
 Holwerda, B. W., Bridge, J. S., Steele, R. L., et al. 2020, *AJ*, **160**, 154
 Huang, K.-H., Ferguson, H. C., Ravindranath, S., et al. 2013, *ApJ*, **765**, 68
 Izotov, Y. I., Schaerer, D., Thuan, T. X., et al. 2016, *MNRAS*, **461**, 3683
 Izotov, Y. I., Schaerer, D., Worseck, G., et al. 2018, *MNRAS*, **474**, 4514
 Jaskot, A. E., Dowd, T., Oey, M. S., et al. 2019, *ApJ*, **885**, 96
 Jaskot, A. E., & Oey, M. S. 2013, *ApJ*, **766**, 91
 Jiang, L., Egami, E., Fan, X., et al. 2013, *ApJ*, **773**, 153
 Jiang, T., Malhotra, S., Rhoads, J. E., et al. 2019a, *ApJ*, **872**, 145
 Jiang, T., Malhotra, S., Yang, H., et al. 2019b, *ApJ*, **872**, 146
 Kennicutt, R. C. 1998, *ApJ*, **498**, 541
 Kim, K., Malhotra, S., Rhoads, J. E., et al. 2020, *ApJ*, **893**, 134
 Kim, K., Oh, S., Jeong, H., et al. 2016, *ApJS*, **225**, 6
 Law, D. R., Steidel, C. C., Erb, D. K., et al. 2007, *ApJ*, **656**, 1
 Liu, C., Mutch, S. J., Poole, G. B., et al. 2017, *MNRAS*, **465**, 3134
 Lotz, J. M., Primack, J., & Madau, P. 2004, *AJ*, **128**, 163
 Malhotra, S., & Rhoads, J. E. 2002, *ApJL*, **565**, L71
 Malhotra, S., Rhoads, J. E., Finkelstein, S. L., et al. 2012, *ApJL*, **750**, L36
 Meert, A., Vikram, V., & Bernardi, M. 2015, *MNRAS*, **446**, 3943
 Meurer, G. R., Heckman, T. M., Lehnert, M. D., Leitherer, C., & Lowenthal, J. 1997, *AJ*, **114**, 54
 Mo, H. J., Mao, S., & White, S. D. M. 1998, *MNRAS*, **295**, 319
 Oesch, P. A., Bouwens, R. J., Carollo, C. M., et al. 2010, *ApJL*, **709**, L21
 Ono, Y., Ouchi, M., Curtis-Lake, E., et al. 2013, *ApJ*, **777**, 155
 Orlitová, I., Verhamme, A., Henry, A., et al. 2018, *A&A*, **616**, A60
 Overzier, R. A., Bouwens, R. J., Cross, N. J. G., et al. 2008, *ApJ*, **673**, 143
 Oyarzún, G. A., Blanc, G. A., González, V., et al. 2017, *ApJ*, **843**, 133
 Paulino-Afonso, A., Sobral, D., Ribeiro, B., et al. 2018, *MNRAS*, **476**, 5479
 Peebles, P. J. E. 1969, *ApJ*, **155**, 393
 Peng, C. Y., Ho, L. C., Impey, C. D., et al. 2002, *AJ*, **124**, 266
 Peng, C. Y., Ho, L. C., Impey, C. D., et al. 2010, *AJ*, **139**, 2097
 Petrosian, V. 1976, *ApJL*, **209**, L1
 Pirzkal, N., Malhotra, S., Rhoads, J. E., et al. 2007, *ApJ*, **667**, 49
 Rhoads, J. E., Malhotra, S., Dey, A., et al. 2000, *ApJL*, **545**, L85
 Rhoads, J. E., Malhotra, S., Richardson, M. L. A., et al. 2014, *ApJ*, **780**, 20
 Ribeiro, B., Le Fèvre, O., Tasca, L. A. M., et al. 2016, *A&A*, **593**, A22
 Ritondale, E., Auger, M. W., Vegetti, S., et al. 2019, *MNRAS*, **482**, 4744
 Rivera-Thorsen, T. E., Dahle, H., Gronke, M., et al. 2017, *A&A*, **608**, L4
 Runnholm, A., Hayes, M., & Melinder, J. 2020, *ApJ*, **892**, 48
 Salpeter, E. E. 1955, *ApJ*, **121**, 161
 Santos, S., Sobral, D., & Matthee, J. 2020, *MNRAS*, **493**, 141
 Shen, S., Mo, H. J., White, S. D. M., et al. 2003, *MNRAS*, **343**, 978
 Shibuya, T., Ouchi, M., & Harikane, Y. 2015, *ApJS*, **219**, 15
 Shibuya, T., Ouchi, M., Harikane, Y., et al. 2019, *ApJ*, **871**, 164
 Shimasaku, K., Fukugita, M., Doi, M., et al. 2001, *AJ*, **122**, 1238
 Taniguchi, Y., Murayama, T., Scoville, N. Z., et al. 2009, *ApJ*, **701**, 915
 Verhamme, A., Orlitová, I., Schaerer, D., et al. 2015, *A&A*, **578**, A7
 Warren, M. S., Quinn, P. J., Salmon, J. K., et al. 1992, *ApJ*, **399**, 405
 Windhorst, R. A., Cohen, S. H., Hathi, N. P., et al. 2011, *ApJS*, **193**, 27
 Wyithe, J. S. B., & Loeb, A. 2011, *MNRAS*, **413**, L38
 Yang, H., Malhotra, S., Gronke, M., et al. 2016, *ApJ*, **820**, 130
 Yang, H., Malhotra, S., Gronke, M., et al. 2017b, *ApJ*, **844**, 171
 Yang, H., Malhotra, S., Rhoads, J. E., et al. 2017a, *ApJ*, **838**, 4